Journal of Materials Chemistry C

ROYAL SOCIETY OF CHEMISTRY

PAPER

View Article Online
View Journal | View Issue



Cite this: J. Mater. Chem. C, 2025, 13, 12745

# Novel scintillators based on cerium-doped garnets in amorphous silica: crystal quality at the cost of glass

Saulius Nargelas,* [a] Monika Skruodienė,[b] Arnoldas Solovjovas,[a] Šarūnas Ščefanavičius,[a] Gabija Soltanaitė,[a] Mantas Migauskas,[a] Žydrūnas Podlipskas,[a] Aivaras Kareiva[b] and Gintautas Tamulaitis [a]

Received 5th March 2025,
Accepted 6th May 2025

DOI: 10.1039/d5tc00985e

rsc.li/materials-c

A two-step sol–gel procedure is proposed to fabricate low-cost composite scintillators consisting of microcrystalline cerium-doped garnets embedded in a silica matrix. Scintillators containing yttrium aluminum garnet (YAG:Ce) and garnets with partial or complete substitution of Y by Lu (LuYAG:Ce and LuAG:Ce) to improve the stopping power of the scintillator were fabricated and studied. X-ray diffraction (XRD) patterns show that the microcrystals exhibit a garnet structure without significant traces of other crystalline phases. Time-resolved photo- and cathodoluminescence spectroscopy revealed that the luminescence is dominated by the emission of unperturbed $Ce^{3+}$ ions, although a small fraction of the emission centers are modified in LuYAG:Ce and LuAG:Ce. The agglomeration of microcrystals with their increasing content in the composite positively influences the luminescence intensity. Despite the relatively low fabrication temperatures, the microcrystals contain trapping centers that reduce the luminescence rate, as observed in the corresponding bulk crystals.



## 1 Introduction

For decades, yttrium aluminum garnet ($Y_3Al_5O_{12}$, YAG) has been the matrix of choice for emitting neodymium ions in the active medium of YAG:Nd lasers, which currently have numerous applications and a billion-dollar market. The renaissance of the YAG matrix, this time for cerium ions, began after the development of bright blue InGaN-based light-emitting diodes (LEDs). YAG:Ce turned out to be an indispensable wavelength converter, transforming the high-efficiency emission of InGaN LED chips at 465 nm into broad-band emission in the yellow region. This enabled the combination of these two spectral components into the simplest and most energy-efficient spectrum for white LEDs, which now dominate the general lighting market and are useful for many other white-light applications.

The YAG:Ce phosphor for white LEDs is particularly attractive due to its exceptionally high internal quantum efficiency (IQE), reported to be as high as 99.5%.[1] However, nonradiative recombination at the surface of YAG:Ce phosphor grains—typically embedded in an epoxy coating of the InGaN chip in conventional white LEDs—reduces the high IQE of the YAG:Ce phosphor. Luminescence efficiency can be improved by applying a silica coating to the YAG:Ce particles. The coating inhibits nonradiative recombination at the particle surface and enhances light extraction from the silica/YAG:Ce interface.[2]

The current study aims to exploit a spillover effect by applying mature practices of developing YAG:Ce as a phosphor in white LEDs to its use as a scintillator. YAG:Ce single crystals were considered to be promising scintillators decades ago;[3] however, a straightforward adoption of these crystals as scintillators faces challenges due to the different modes of excitation in the modes of operation as phosphors and as scintillators: resonant photoexcitation to the emitting $5d^1$ level of the activator ion $Ce^{3+}$ in white LEDs and excitation by high-energy photons or particles in scintillation detectors of ionizing radiation. In the latter case, excitation transfer to the activator ion becomes important. Some of these excitations may be captured by centers of nonradiative recombination. In particular, the YAG matrix has shallow traps that play no role in the resonant photoexcitation of $Ce^{3+}$, but substantially reduce the light emission efficiency at high-energy excitations by channeling a portion of the relaxed electrons and holes to the centers of nonradiative recombination.

Fortunately, the garnet matrix is quite flexible and can accommodate ions of different radii without substantial deterioration of the garnet lattice. As a result, multicomponent garnet matrices have been developed to successfully exploit

[a] Vilnius University, Institute of Photonics and Nanotechnology, 10257 Vilnius, Lithuania. E-mail: saulius.nargelas@ff.vu.lt
[b] Vilnius University, Institute of Chemistry, Department of Inorganic Chemistry, 03225 Vilnius, Lithuania

band gap engineering to bury the undesirable trapping levels in the conduction band[4,5] and to engineer the localized energy levels that enable a downshift of the emitting level of $Ce^{3+}$ to increase the energy barrier for thermal depopulation of the level.[6,7] The best current multicomponent garnet matrix for $Ce^{3+}$ in scintillators is gadolinium gallium aluminum garnet (GAGG), which has a high light yield, reported to be up to 46 000 photons per MeV,[8] relatively fast response, and high radiation tolerance. Unfortunately, the growth of GAGG single crystals requires high temperatures, and only expensive iridium crucibles are sufficiently resistant for growth under such conditions. This is a major issue in the production of GAGG:Ce for the two major markets of scintillation detectors: particle physics experiments, which typically require tens of thousands of large scintillation crystals, and medical imaging, especially time-of-flight positron emission tomography (TOF-PET) devices, where scintillation crystals account for about two-thirds of the total cost.

Fabricating Ce-doped garnet ceramics is less expensive than growing single crystals and enables a higher content of activator ions. Thin GAGG:Ce may even exhibit a higher scintillation light yield compared to the corresponding single crystal.[9] However, fabricating high-efficiency transparent ceramics becomes both difficult and expensive,[10] and the afterglow in ceramic scintillators remains another important challenge.[11] Cerium-doped glasses offer a promising alternative as inexpensive scintillators, benefiting from the mature glass industry that can easily scale their production. Ce-doped Ba–Gd silica glass[12] or $SiO_2$:$Ce^{3+}$ glass[13] has exhibited promising results, though excitation transfer to the emitting $Ce^{3+}$ ions in these glasses remains a significant challenge in the development of efficient glass scintillators. Composite scintillators containing single-crystal micrograins of the scintillating material dispersed in a host matrix represent another approach.[14,15] The potential of this approach in the fabrication of scintillators for X-ray imaging has been recently demonstrated for Ce-doped gadolinium aluminum gallium garnet powders dispersed in a polysiloxane matrix.[16] However, the calcination of the garnets can be performed in expensive iridium crucibles due to the high temperatures required for the process.

In this study, we aim to develop a low-cost scintillator based on Ce-doped garnets by fabricating microcrystalline YAG:Ce in a silica matrix. This approach exploits (i) the efficient excitation transfer to the emitting $Ce^{3+}$ ions *via* the YAG matrix within the microcrystals, (ii) the expected passivation of the microcrystal surface by silica, and (iii) the inexpensive and flexible sol–gel technique for fabricating the composite scintillator. The viability of the sol–gel technique has already been demonstrated in the synthesis of the composite phosphor materials.[17] In the current study, we also fabricated a composite scintillator with lutetium substituting yttrium in the garnet matrix. The heavy Lu increases the stopping power of the scintillator for hard X-ray and gamma radiations due to a higher density and effective atomic number of LuAG (6.67 g $cm^{-3}$ and $Z_{eff}$ = 63) compared to those of YAG (4.56 g $cm^{-3}$ and $Z_{eff}$ = 32.6).

# 2 Experimental

## 2.1 Sample preparation

The composite materials consisting of either YAG:Ce, YLuAG:Ce, or LuAG:Ce nanocrystals in a silica matrix were fabricated in two steps: synthesis of Ce-doped garnet powder and synthesis of the composite scintillator. A sol–gel synthesis technique was used in both steps.

The Ce-doped garnet nanocrystals were synthesized using the following precursors: $Y_2O_3$ and/or $Lu_2O_3$ (99.9%, Alfa Aesar) and $Al(NO_3)_3{\cdot}9H_2O$ (99.999%, Alfa Aesar), $(NH_4)_2Ce(NO_3)_6$ (99.5%, Roth), and $H_3BO_3$ (99.5%, ChemPur). First, $Y_2O_3$ or/and $Lu_2O_3$ were dissolved in a hot concentrated nitric acid at 80 °C. Then, the acid was evaporated, and the residual gel was washed three times with approximately 200 mL of distilled water, followed by the evaporation of water. Afterwards, an additional 50 mL of distilled water was added and three precursors, $Al(NO_3)_3{\cdot}9H_2O$, $(NH_4)_2Ce(NO_3)_6$, and $H_3BO_3$, were dissolved in proportions to achieve a nominal Ce content of 0.5% in the garnet. The solution was left under magnetic stirring for 2 hours at 50 °C. Citric acid was added to the solution in a molar ratio of 1 : 1 to the metal ions and stirred overnight. The solution was evaporated at the same temperature of 50 °C. The obtained gel was dried for 24 hours at a temperature of 140 °C. After that, the obtained xerogel was heated at 600 °C for 2 hours to remove any organic residue. Next, the porous xerogel was ground in a mortar and annealed at two different temperatures. Then, it was calcined to 1000 °C for 2 hours at a heating rate of 5 °C $min^{-1}$ in covered crucibles in air. Subsequently, the same powders were ground again in a mortar and annealed to 1200 °C for 4 hours in air at the same heating rate of 5 °C $min^{-1}$.

The composite material containing the ground scintillator material fabricated in the first step was synthesized using the sol–gel synthesis method with modified gelation and drying processes to obtain a crack-free material, as suggested by Kajihara.[18] Initially, a hydrolysis reaction was performed at room temperature between the silicon organic precursor tetraethoxysilane (TEOS) (99.0%, Sigma-Aldrich) and deionized water containing a small amount of nitric acid ($HNO_3$) (65.0%, Sigma-Aldrich) and a certain amount of scintillator powder. The molar ratio of $TEOS : H_2O : HNO_3$ was 1 : 22 : 0.002. The mixture was stirred for 1 hour at room temperature to obtain a homogeneous solution with the pH of the sol maintained between 1 and 2. Ammonium acetate ($AcONH_4$) (97.0%, Sigma-Aldrich) buffer solution prepared in deionized water was added to adjust the pH to 5–6, followed by stirring the obtained sol for an additional 2 minutes at room temperature. Afterward, the sol was immediately transferred to a drying container placed in an ultrasonic bath to prevent the formation of air bubbles, which could lead to gel cracking, and was left there for 30 minutes. Subsequently, the sol was gradually dried in a drying oven, with slowly increasing the temperature from room temperature to 70 °C. The entire drying process lasted 168 hours. The obtained xerogels YAG:Ce/$SiO_2$, YLuAG:Ce/$SiO_2$ and LuAG:Ce/$SiO_2$ were placed in a quartz tube furnace and annealed in a He

 

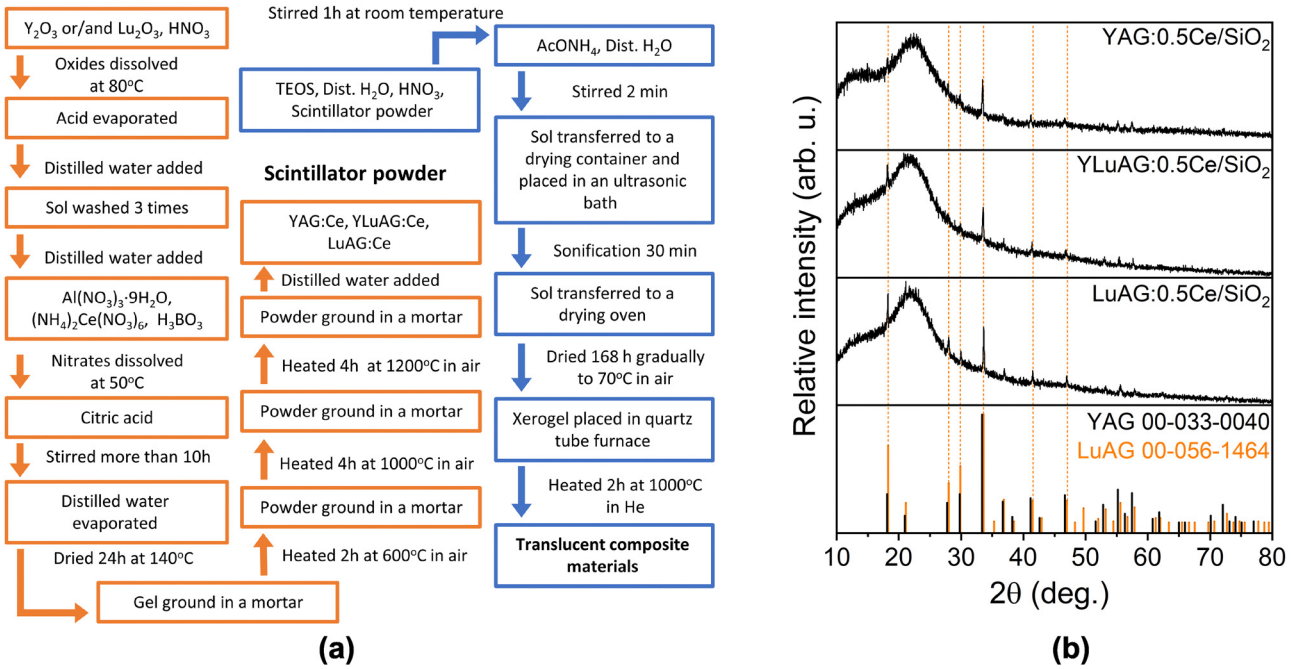


Fig. 1 (a) Scheme of sol–gel synthesis of composite scintillators consisting of Ce-doped garnets in a silica matrix. (b) XRD patterns of composite samples containing 0.5 wt% YAG:Ce, LuYAG:Ce, and LuAG:Ce, and PDF data for the corresponding single crystals.

atmosphere to 1000 °C for 2 hours at a heating rate of 5 °C $min^{-1}$. As a result, translucent YAG:Ce/$SiO_2$, YLuAG:Ce/$SiO_2$ and LuAG:Ce/$SiO_2$ composite materials were obtained. Improving optical transparency by optimizing the annealing process was beyond the scope of the current study. The key features of the fabrication process are schematically summarized in Fig. 1a.

### 2.2 Characterization techniques

In photoluminescence experiments, the wavelength-tunable output of an optical parametric amplifier (Orpheus, Light Conversion) pumped by a Yb:KGW femtosecond laser (Pharos, Light Conversion) emitting 170 fs pulses at a wavelength of 1030 nm was used as an excitation source for photoluminescence (PL), time-resolved photoluminescence (TRPL), and quantum yield (QY) measurements. Emission spectra were recorded using a 328-mm-focal-length spectrograph (Kymera 328i, Andor) equipped with a UV-VIS BT-CCD camera (Hamamatsu) for PL measurements and with a UV-VIS streak camera (C10910-01, Hamamatsu) ensuring 30 ps time resolution for TRPL measurements. The estimation of QY was carried out using a 6-inch-diameter integrating sphere (Gigahertz Optik) coated with $BaSO_4$ and applying the three-measurement method described in ref. 19.

Cathodoluminescence (CL) experiments were carried out using an Attolight Chronos spectrometric system, enabling measurements with spatial, spectral, and temporal resolution. The samples were excited by short electron pulses accelerated at a voltage of 10 kV, generated by triggering the electron gun with a sub-10-ps laser (aeroPULSE PS, NKT Photonics). The luminescence was collected using a Cassegrain-type objective connected to a spectrometer (iHR 320, Horiba) and recorded using either a streak camera (Hamamatsu C10910) for transient capture or a charge-coupled device (CCD) camera (Newton 920, Andor) for spatial mapping. To achieve the optimal time resolution of 100 ps, the luminescence decay was reconstructed using the results obtained from multiple temporal-window measurements at a pulse repetition rate of 2 MHz. Spatial maps of time-integrated cathodoluminescence and scanning electron microscopy (SEM) images were captured in CW operation mode using an electron probe enabled by Schottky emission.

The phase purity of the microcrystals in the composite material was studied using a Rigaku MiniFlex II X-ray diffractometer (XRD) with Ni-filtered Cu K$\alpha$1 radiation. The XRD images were collected in the $2\theta$ range between 150° and 800° at a step of 0.01°, a scan speed of 10° $min^{-1}$, and a dwell time of 5.0 s.

All measurements were performed at room temperature.

## 3 Results

Three sets of samples containing Ce-doped garnets in silica – YAG/$SiO_2$, LuYAG/$SiO_2$, and LuAG/$SiO_2$ – were prepared. Each set consisted of four samples with garnet contents of 0.5, 1, 1.5, and 2 wt%.

### 3.1 Structural characterization

The XRD patterns of the composite samples containing 0.5 wt% YAG:Ce, LuYAG:Ce, and LuAG:Ce are presented in Fig. 1b. The broad band in the range from 20° to 30° is characteristic of amorphous $SiO_2$. A comparison of the narrow lines with those in the powder diffraction files (PDFs) for YAG and LuAG

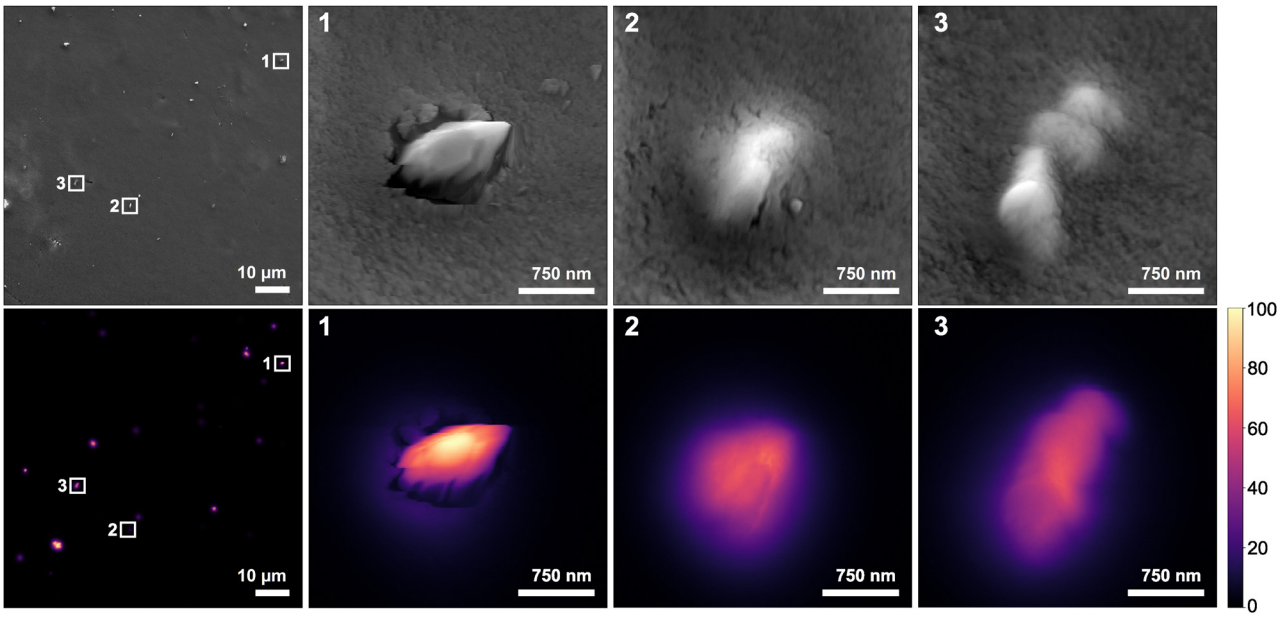


Fig. 2 Scanning electron microscopy (SEM) images (upper row) and cathodoluminescence intensity maps (lower row) of the YAG:Ce/$SiO_2$ sample containing 2 wt% YAG:Ce. The spots presented at a higher magnification in subsequent columns are indicated by numbers in the images provided in the first column.

(#00-033-0040 and #00-056-1464, respectively) confirms the absence of crystal phases other than the garnet in amorphous silica. The XRD peaks for LuYAG/$SiO_2$ lie between the corresponding peaks for YAG and LuYAG single crystals. No significant deviations from the garnet structure were observed in any of the samples studied.

SEM images of selected emitting structures in the YAG:Ce/$SiO_2$ sample containing 2 wt% YAG:Ce are presented in Fig. 2, along with the cathodoluminescence intensity maps of the same sample areas. The mapping indicates that the YAG:Ce/$SiO_2$ composite scintillators, fabricated as described above, contain submicrometer grains that tend to agglomerate. The formation of these agglomerates is beneficial for higher emission intensity. Agglomeration becomes more pronounced as the YAG:Ce content in the YAG:Ce/$SiO_2$ composite scintillator increases. Similar trends were observed in the SEM and CL mappings for LuAG:Ce/$SiO_2$ and LuYAG:Ce/$SiO_2$.

### 3.2 Photoluminescence study

The photoluminescence spectra of YAG:Ce/$SiO_2$ and LuAG:Ce/$SiO_2$ samples, recorded under resonant excitation (450 nm) to the $5d^1$ levels of $Ce^{3+}$, are compared with the spectra of the corresponding single crystal (SC) and single-crystal film (SCF) recorded under the same conditions, as shown in Fig. 3a. No significant deviations between the $Ce^{3+}$ emission spectra of the composite material and those of the single crystal are observed. As expected, the spectrum consists of two strongly overlapping bands due to optical transitions to the two ground-state levels, $F_{7/2}$ and $F_{5/2}$. The shift of 25 nm in the spectral position of the bands for $Ce^{3+}$ in YAG and LuAG is attributed to the different strengths of the crystal field at the site of the emitting ion. The coincidence of the spectra for the composite material and the single crystal of the same garnet indicates that the crystal field experienced by $Ce^{3+}$ in the microcrystals is identical to that in a single crystal.

The possible contribution of $SiO_2$ emission to the emission spectra of the composite scintillator was studied for excitation at 346 nm, corresponding to excitation to the second excited level $5d^2$ of $Ce^{3+}$. No significant differences between the spectra of $Ce^{3+}$ ions under excitation to $5d^2$ and $5d^1$ were observed. Meanwhile, photons at 346 nm excite a band with a peak at 414 nm. Although the band gap of $SiO_2$ (which depends on polymorphs but is around 9 eV for all of them[20]) is substantially larger than the excitation photon energy of 3.58 eV, the photons likely excite certain defect-related centers of radiative recombination. It is worth noting that the band with a peak at 414 nm and the emission of $Ce^{3+}$ are well separated spectrally. Moreover, the band in $SiO_2$ decays substantially faster than the Ce-related band in the garnet (see the inset in Fig. 3b). A rough fit of the decays by single exponents provides decay constants of 60 and 14 ns, respectively.

The PL intensity dependence on the scintillator content in the composite samples is shown in Fig. 3c for all three garnets studied. The intensity increases linearly at low scintillator contents but exhibits a superlinear increase at higher contents. This feature is especially pronounced in LuYAG:Ce/$SiO_2$.

The quantum efficiency as a function of the scintillator content in the composite with amorphous silica is presented for all three sets of samples in Fig. 3d. The measurements were carried out under resonant photoexcitation to the emitting $5d^1$ level of $Ce^{3+}$ ions. The dependence shows a trend of increasing efficiency with increasing scintillator content. This tendency is most pronounced in the composites containing LuYAG:Ce and gradually ceases at higher garnet contents in all three sets of

 

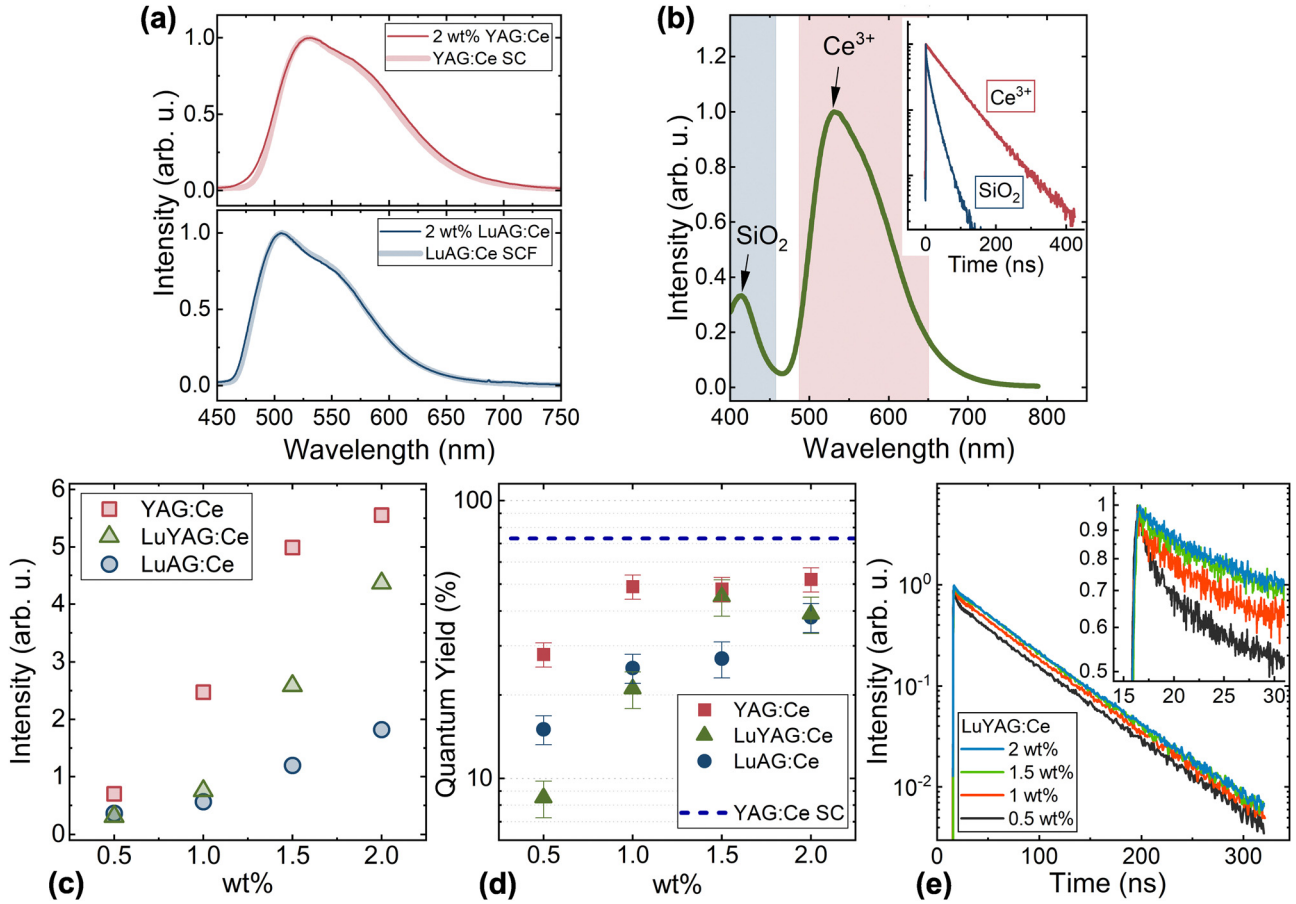


Fig. 3 (a) Normalized photoluminescence spectra of YAG:Ce/$SiO_2$ and LuAG:Ce/$SiO_2$ samples containing 2 wt% of the scintillator material (thin solid lines) and of the corresponding single crystal (SC) and single-crystal film (SCF) (thick lines) under resonant excitation (450 nm) to $5d^1$ levels of $Ce^{3+}$. (b) Photoluminescence spectrum of YAG:Ce/$SiO_2$ for excitation at 346 nm. In the inset, the PL decay kinetics are shown for two luminescence bands corresponding to the emission of $Ce^{3+}$ and the $SiO_2$ of the composite material. (c) Photoluminescence intensity under excitation to the $5d^1$ (450 nm) level of $Ce^{3+}$ as a function of scintillator content. (d) Quantum yield of samples with different amounts of YAG:Ce, LuAG:Ce, and LuYAG:Ce. The QY of the YAG:Ce single crystal is indicated by a horizontal dashed line. (e) Photoluminescence decay in samples with different LuYAG:Ce contents (indicated) under excitation to the $5d^1$ level of $Ce^{3+}$. The initial part of the decay is extended in the inset.

samples with different garnet contents studied. The absolute quantum efficiency values of the composite scintillators studied (40–50%) is still lower than but comparable to that measured under the same conditions in bulk YAG:Ce (80%).

The major part of the photoluminescence in the composite samples with all three types of Ce-doped garnets decays exponentially (see Fig. 3e) at the same rate as in bulk crystals (the characteristic decay time is 60 ns). However, the initial part of the decay in LuYAG:Ce and LuAG:Ce exhibits a fast component. This fast decay component is more pronounced in the samples containing low garnet content, as shown in the inset of Fig. 3e. The PL decay in the samples under study fitted well with a biexponential function with the decay constant of the slow component fixed at 60 ns for all the samples. The decay constants and weight coefficients of the components are listed in Table 1.

Table 1 Decay times extracted from the best biexponential fits of photoluminescence and cathodoluminescence kinetics in composite scintillators YAG:Ce/($SiO_2$), LuAG:Ce/($SiO_2$) and LuYAG:Ce/($SiO_2$) with a garnet content of 2 wt%. The weight coefficients of fast and slow components are indicated in brackets

| | Decay time (ns) | | | |
|---|---|---|---|---|
| | Photoluminescence | | Cathodoluminescence | |
| | Fast | Slow | Fast | Slow |
| YAG:Ce | — | 60 (100%) | — | 85 (100%) |
| LuYAG:Ce | 37 (12%) | 60 (88%) | 25 (55%) | 85 (45%) |
| LuAG:Ce | 37 (32%) | 60 (68%) | 25 (58%) | 85 (42%) |

### 3.3 Cathodoluminescence kinetics

A typical CCD image showing the time evolution of the cathodoluminescence spectrum in YAG:Ce/$SiO_2$ is presented in Fig. 4a, along with two cross-sections of the image showing the time-integrated CL spectrum and the time evolution of spectrally-integrated CL intensity. The CL and PL band peak positions and shapes for $Ce^{3+}$ emission are very similar in all the samples studied. The CL spectra collected over a broader spectral range from a few microcrystals are compared in Fig. 4b. All the spectra are identical, showing that the microcrystal shape and size have

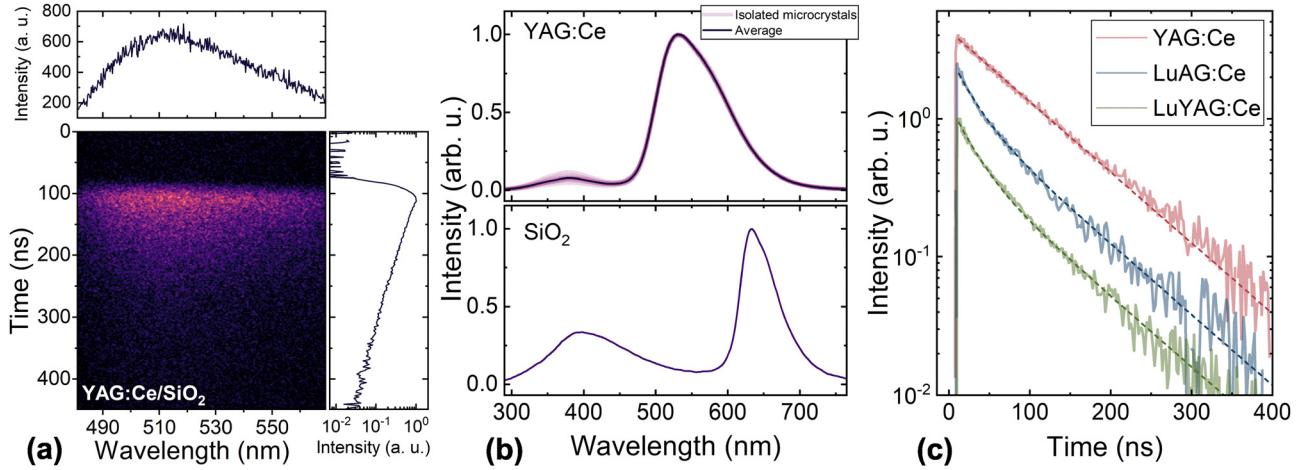


Fig. 4 (a) CCD image showing the time evolution of the cathodoluminescence spectrum in YAG:Ce/$SiO_2$, with the time-integrated spectrum shown above and the spectrally-integrated kinetics shown beside. (b) Cathodoluminescence spectra collected selectively from 9 microcrystals and their average in the YAG:Ce/$SiO_2$ composite (top) and from the composite areas containing no garnet microcrystals (bottom). (c) Cathodoluminescence decays in YAG:Ce/$SiO_2$, LuAG:Ce/$SiO_2$, and LuYAG:Ce/$SiO_2$ (solid lines as indicated) and the best fits for them as described in the text (dashed lines as indicated).

no significant influence on the spectra. In addition to the band caused by $Ce^{3+}$ emission, two more luminescence bands are observed. These bands are caused by the emission from silica, as they are also observed in the CL spectra collected from areas containing no garnet microcrystals (see Fig. 4b (bottom part)).

The CL of $Ce^{3+}$ in YAG:Ce/$SiO_2$ decays exponentially (see Fig. 4c) with a decay time of 85 ns. The CL in LuAG:Ce/$SiO_2$ and LuYAG:Ce/$SiO_2$ exhibits a similar decay rate for delays longer than 150 ns but also has a faster decay component. The decays in these two composite materials were fitted using a biexponential function, with the slower decay time fixed at 85 ns. The best fits were achieved with the same decay time of 25 ns for the fast component in both LuAG:Ce/$SiO_2$ and LuYAG:Ce/$SiO_2$ (see Table 1).

## 4 Discussion

The XRD patterns of the composite scintillators consisting of YAG:Ce, LuYAG:Ce, and LuAG:Ce microcrystals in the silica matrix evidence the coexistence of single-phase garnets and amorphous silica. This experimental observation confirms that no significant contamination of garnet microcrystals with silicon occurs during the sol–gel procedures used to fabricate the compound scintillators consisting of Ce-doped garnets in silica. Silicon in YAG acts as a tetravalent impurity ($Si^{4+}$) and facilitates the formation of the perovskite phase.[21]

SEM images and CL maps show that the composite scintillators contain micrometer-sized grains of Ce-doped garnet in a silica matrix, and some of the grains are agglomerated into clusters. An increase in garnet content in the composite is favorable for agglomeration, usually leading to luminescence quenching. In contrast, the luminescence intensity in the composites increases faster than the garnet content, at least up to 2 wt%, which was the highest garnet content in the current study. This feature warrants dedicated optimization to fabricate composites with a garnet content above 2 wt% in order to produce scintillators with higher stopping power for ionizing radiation detection.

To reveal the influence of the grain size on the emission intensity, we performed a statistical analysis of CL data for individual grains. The distribution of the CL intensities from individual grains according to their area is presented in Fig. 5. Since the shape of the grains is irregular, we estimated the grain area by counting its CL scan pixels emitting at an intensity above a fixed limit. The luminescence intensities of each pixel counted as emitting for the individual grain were summed up and divided by the grain area. Thus, each point in Fig. 5 represents the CL intensity of an individual grain normalized to its area. Consequently, in the case of the emission proportional only to the grain area, all points in Fig. 5 should have the same value on the *Y*-axis. Instead, we observe an increase in the normalized intensity as the grain size increases for all samples studied. This behavior might be interpreted by an increase in the volume-to-surface ratio as the grain size increases. The surface usually contains centers of nonradiative recombination, and thus the influence of the surface-related nonradiative recombination decreases in larger grains.

The quantum efficiency of $Ce^{3+}$ luminescence, excited selectively to the lowest emitting level $5d^1$, increases with increasing garnet content at low concentrations and tends to saturate at higher concentrations (see Fig. 3d). The increase might be interpreted by agglomeration of the grains in larger clusters, provided that the surfaces between two grains in the cluster contain less nonradiative recombination centers than the surfaces between the grains and silica. It is worth noting that the increase of quantum efficiency saturates at elevated garnet contents in the composite, whereas the overall photoluminescence intensity continues growing superlinearly with the increasing garnet content (see Fig. 3c). This feature could be

 

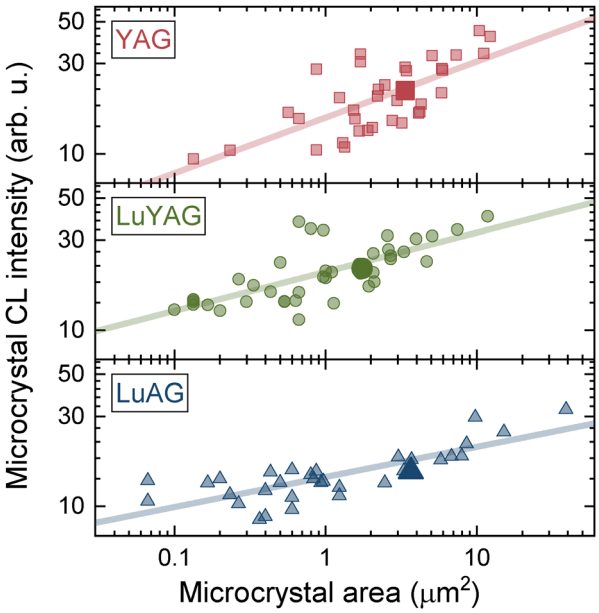


Fig. 5 Cathodoluminescence intensity of individual grains, normalized to their area, *versus* the area for composite scintillators YAG:Ce/$SiO_2$, LuAG:Ce/$SiO_2$, and LuYAG:Ce/$SiO_2$ (as indicated) containing 2 wt% of the scintillating material. Solid points indicate the mean values of the grains analyzed in the samples.

attributed to improved light extraction due to enhanced scattering of luminescence light.

It is worth noting that the internal quantum efficiency of $Ce^{3+}$ emission (see Fig. 3d) is close to that in the corresponding single crystals but still has potential for further improvement, possibly by optimizing the sol–gel procedures developed in the current study.

The emission spectra of the activator ion $Ce^{3+}$ in the composite scintillators are actually identical to those in the corresponding single crystal garnets. This indicates that no significant changes in the crystal field experienced by the emitting $Ce^{3+}$ occur in the submicrometer-sized garnet microcrystals formed in silica. This is consistent with the results of structural analysis, which evidence just one crystalline phase, and the relatively high quantum efficiency, indicating no substantial influence of structural defects or impurities, at least in the close proximity of the emitting Ce ions.

The luminescence spectra of the composite scintillators under study also contain broad bands due to radiative recombination at defect-related emission centers in the silica matrix. The silica-related UV band in PL spectra weakly overlaps with the $Ce^{3+}$ emission (see Fig. 3b). The two silica-related bands observed in the CL spectra of the composite scintillators are also spectrally separated from the $Ce^{3+}$ emission. The spectral positions of the two bands correspond to those observed in the CL spectra of $SiO_2$ layers of different thicknesses deposited on silicon.[22] The silica-related UV bands observed in PL (see Fig. 3b) and CL spectra peak at different positions, as already observed in $SiO_2$ and interpreted by the different excitation conditions of photons and high-energy electrons.[22] The decay of the silica photoluminescence is substantially faster than that of $Ce^{3+}$ emission (see the inset in Fig. 3b). Thus, the emission of silica in the composite scintillators under study is spectrally separated from the useful emission in the Ce-doped garnet microcrystals and decays substantially faster. Consequently, the silica emission can be eliminated by an appropriate arrangement of scintillation detection.

The CL and PL kinetics in composite scintillators YAG:Ce/$SiO_2$, LuAG:Ce/$SiO_2$, and LuYAG:Ce/$SiO_2$, as well as their bulk crystal analogs, are compared in Fig. 6. The PL and CL intensities in YAG:Ce/$SiO_2$ decrease nearly exponentially but with different decay constants, 60 ns and 85 ns for PL and CL, respectively. A similar difference in CL and PL decays was observed in GAGG:Ce and interpreted by a delayed excitation transfer *via* the subsystem of Gd ions in the GAGG matrix.[23] However, the delay in excitation transfer to the emitting $Ce^{3+}$ ions after excitation with high energy electrons in YAG:Ce is most probably caused by carrier trapping. A difference in

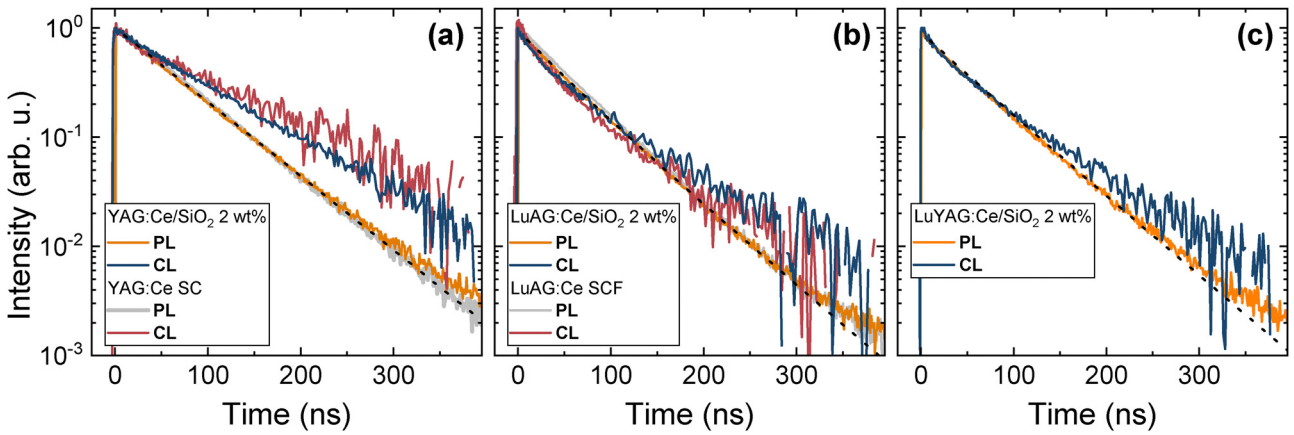


Fig. 6 Cathodoluminescence (CL) and photoluminescence (PL) kinetics (as indicated) in composite scintillators YAG:Ce/$SiO_2$ (a), LuAG:Ce/$SiO_2$ (b), and LuYAG:Ce/$SiO_2$ (c) with a garnet content of 2 wt%. The kinetics for the corresponding single crystal (indicated as SC) and single-crystal film (SCF) are provided for comparison. The best biexponential fits are indicated by black dashed lines.

luminescence decay rates in YAG:Ce after optical and gamma excitation has been observed at room temperature and interpreted by trapping of electrons migrating to the emitting $Ce^{3+}$ centers.[24]

Many types of intrinsic and impurity-related defects are theoretically predicted in YAG; some of them have low activation energies and might act as traps.[21] Thermoluminescence glow curves of YAG:Ce show that up to 11 shallow traps might be effective in YAG:Ce.[24] The trapping centers in YAG:Ce might have various origins. Theoretical studies show that antisite defects $Y_{Al}^{3+}$ are the lowest-energy intrinsic defects in both YAG and LuAG,[21] and a high density of these defects is experimentally evidenced in typical YAG single crystals grown at high temperatures (1800–1900 °C).[25] However, the density of such defects is shown to be substantially lower in thin layers grown by liquid phase epitaxy at lower temperatures (850–1100 °C)[26] and in ceramics sintered at temperatures much lower than the melting point of YAG.[27] Thus, the influence of the antisite defects as electron traps is hardly significant in our samples fabricated at moderate temperatures using the sol–gel technique. The origin of the trapping centers requires a dedicated study.

The introduction of lutetium in the garnet structure results in the emergence of a fast decay component. A fast decay component was previously observed in GAGG[28] and lutetium gadolinium gallium aluminum garnets[29] codoped with Ce and Mg and interpreted by the formation of $Ce^{3+}$ centers modified by Mg ions in close proximity to $Ce^{3+}$. Similarly, the introduction of Lu might facilitate the formation of modified $Ce^{3+}$ emission centers with an enhanced rate of nonradiative recombination that reduces the population of the emitting $5d^1$ level in $Ce^{3+}$ and, consequently, increases the luminescence decay rate. The fast luminescence decay component due to the enhanced nonradiative recombination is more pronounced in the samples containing a lower garnet content (see the inset in Fig. 3e). This is consistent with the lower internal quantum efficiency observed in these samples.

## Conclusions

We demonstrated that the proposed two-step sol–gel procedures enable the fabrication of a low-cost composite scintillator consisting of microcrystalline YAG:Ce, LuYAG:Ce, and LuAG:Ce in a silica matrix. We found that the cathodoluminescence intensity of an individual micrograin grows faster than the grain area and attribute this behavior to the reduced influence of nonradiative surface recombination as the volume-to-surface ratio increases in larger grains.

The emitting $Ce^{3+}$ ions in the garnet-type microcrystals of the composite scintillator experience a crystal field of the same value as in the corresponding bulk single crystals. The luminescence in YAG:Ce, LuYAG:Ce, and LuAG:Ce microcrystals is dominated by the emission of unperturbed $Ce^{3+}$ ions. A fast decaying component in the luminescence is observed in Lu-containing samples and is interpreted by the Lu-facilitated formation of modified emission centers consisting of $Ce^{3+}$ ions and defects in their close proximity.

The silica matrix has defect-related centers of radiative recombination emitting certain background light that is undesirable in the performance of the composite material as a scintillator. Fortunately, our results show that the silica luminescence is spectrally well separated from the useful emission of $Ce^{3+}$ ions and decays much faster. Therefore, the influence of the silica matrix on the emission of the compound scintillator might be eliminated by an appropriate arrangement of scintillation detection.

The observed difference in the luminescence decay rates after excitation by high-energy electrons and photons resonantly to the emitting level $5d^1$ of $Ce^{3+}$ ions shows that a significant concentration of trapping centers are formed in the garnet microcrystals, despite the relatively low temperatures employed in the sol–gel procedures to fabricate the compound scintillator. Since the formation of antisite defects that are the most probable intrinsic defects in garnets is strongly reduced by the low temperatures employed in the sol–gel procedures developed in this study, a dedicated study of the origins of the trapping centers and the possible ways to diminish their density is necessary for further improvement of the composite scintillators.

With increasing content of the Ce-doped garnet in the composite scintillator, the quantum efficiency of the emitting $Ce^{3+}$ ions initially increases and saturates at a level close to the quantum efficiency of single crystal YAG:Ce. Meanwhile, the overall luminescence intensity grows superlinearly with the increase in the garnet content in the range of up to 2 wt% of the samples studied. Thus, a dedicated optimization of the fabrication conditions is promising to improve the emission efficiency up to the level sufficient for applications.

## Author contributions

S. Nargelas: investigation, formal analysis, software, visualization, writing – review & editing; M. Skruodienė: sample preparation, investigation, formal analysis, visualization, writing – review & editing; A. Solovjovas: investigation, formal analysis; Š. Ščefanavičius: investigation, formal analysis; G. Soltanaitė: investigation, formal analysis; M. Migauskas: software, formal analysis; Ž. Podlipskas: investigation, software, formal analysis, visualization, writing – review & editing; A. Kareiva: funding acquisition, resources, writing – review & editing; G. Tamulaitis: funding acquisition, supervision, writing – original draft, writing – review & editing. All authors have read and approved the final version of the manuscript.

## Data availability

The data supporting the findings of this study can be obtained from the corresponding author upon request.

 

## Conflicts of interest

There are no conflicts to declare.

## Acknowledgements

This research has been carried out within the framework of the ''Universities' Excellence Initiative'' programme by the Ministry of Education, Science and Sports of the Republic of Lithuania under the agreement with the Research Council of Lithuania (project no. S-A-UEI-23-6).

## Notes and references

1 S. Akiyama, R. Moriyama, R. Miya, T. Tanaka, J. Tanaka, Y. Sato, K. Tomita, M. Kakihana and H. Kato, *Opt. Mater.*, 2022, **128**, 112386.
2 Y. Nien, K. Chen and I. Chen, *J. Am. Ceram. Soc.*, 2010, **93**, 1688–1691.
3 M. Moszyński, T. Ludziejewski, D. Wolski, W. Klamra and L. Norlin, *Nucl. Instrum. Methods Phys. Res., Sect. A*, 1994, **345**, 461–467.
4 M. Fasoli, A. Vedda, M. Nikl, C. Jiang, B. P. Uberuaga, D. A. Andersson, K. J. McClellan and C. R. Stanek, *Phys. Rev. B:Condens. Matter Mater. Phys.*, 2011, **84**, 081102.
5 S. K. Yadav, B. P. Uberuaga, M. Nikl, C. Jiang and C. R. Stanek, *Phys. Rev. Appl.*, 2015, **4**, 054012.
6 K. Kamada, T. Endo, K. Tsutumi, T. Yanagida, Y. Fujimoto, A. Fukabori, A. Yoshikawa, J. Pejchal and M. Nikl, *Cryst. Growth Des.*, 2011, **11**, 4484–4490.
7 K. Kamada, T. Yanagida, J. Pejchal, M. Nikl, T. Endo, K. Tsutumi, Y. Fujimoto, A. Fukabori and A. Yoshikawa, *J. Phys. D: Appl. Phys.*, 2011, **44**, 505104.
8 K. Kamada, T. Yanagida, J. Pejchal, M. Nikl, T. Endo, K. Tsutsumi, Y. Fujimoto, A. Fukabori and A. Yoshikawa, *IEEE Trans. Nucl. Sci.*, 2012, **59**, 2112–2115.
9 T. Yanagida, K. Kamada, Y. Fujimoto, H. Yagi and T. Yanagitani, *Opt. Mater.*, 2013, **35**, 2480–2485.
10 C. Dujardin, E. Auffray, E. Bourret-Courchesne, P. Dorenbos, P. Lecoq, M. Nikl, A. N. Vasil'ev, A. Yoshikawa and R.-Y. Zhu, *IEEE Trans. Nucl. Sci.*, 2018, **65**, 1977–1997.
11 Y. Tang, M. Qiang, W. Lou, Y. Ding, H. Lin, R. Hong and D. Zhang, *Ceram. Int.*, 2024, **50**, 36286–36294.
12 V. Dormenev, A. Amelina, E. Auffray, K.-T. Brinkmann, G. Dosovitskiy, F. Cova, A. Fedorov, S. Gundacker, D. Kazlou, M. Korjik, N. Kratochwil, V. Ladygin, V. Mechinsky, M. Moritz, S. Nargelas, R. Novotny, P. Orsich, M. Salomoni, Y. Talochka, G. Tamulaitis, A. Vaitkevicius, A. Vedda and H.-G. Zaunick, *Nucl. Instrum. Methods Phys. Res., Sect. A*, 2021, **1015**, 165762.
13 N. Chiodini, M. Fasoli, M. Martini, E. Rosetta, G. Spinolo, A. Vedda, M. Nikl, N. Solovieva, A. Baraldi and R. Capelletti, *Appl. Phys. Lett.*, 2002, **81**, 4374–4376.
14 V. A. Litichevskyi, A. D. Opolonin, S. N. Galkin, A. I. Lalaiants and E. F. Voronkin, *Instrum. Exp. Tech.*, 2013, **56**, 436–443.
15 V. Litichevskyi, *Funct. Mater.*, 2013, **20**, 259–265.
16 I. Gerasymov, T. Nepokupnaya, A. Boyarintsev, O. Sidletskiy, D. Kurtsev, O. Voloshyna, O. Trubaieva, Y. Boyarintseva, T. Sibilieva, A. Shaposhnyk, O. Opolonin and S. Tretyak, *Opt. Mater.*, 2020, **109**, 110305.
17 M. Skruodiene, M. Kemere, G. Inkrataite, M. Leimane, R. Ramanauskas, R. Skaudzius and A. Sarakovskis, *Gels*, 2023, **9**, 488.
18 K. Kajihara, *J. Asian Ceram. Soc.*, 2013, **1**, 121–133.
19 S. Leyre, E. Coutino-Gonzalez, J. J. Joos, J. Ryckaert, Y. Meuret, D. Poelman, P. F. Smet, G. Durinck, J. Hofkens, G. Deconinck and P. Hanselaer, *Rev. Sci. Instrum.*, 2014, **85**, 123115.
20 D. Denice, A. Arya, M. Kumar and G. Vinod, *Mater. Today Commun.*, 2022, **31**, 103607.
21 M. M. Kuklja, *J. Phys.: Condens. Matter*, 2000, **12**, 2953–2967.
22 A. Baraban, S. Samarin, V. Prokofiev, V. Dmitriev, A. Selivanov and Y. Petrov, *J. Lumin.*, 2019, **205**, 102–108.
23 Y. Talochka, S. Nargelas, Ž. Podlipskas, M. Kucera, Z. Lucenicova and G. Tamulaitis, *Radiat. Phys. Chem.*, 2024, **218**, 111589.
24 E. Zych, C. Brecher and J. Glodo, *J. Phys.: Condens. Matter*, 2000, **12**, 1947–1958.
25 Y. Zorenko, A. Voloshinovskii, V. Savchyn, T. Voznyak, M. Nikl, K. Nejezchleb, V. Mikhailin, V. Kolobanov and D. Spassky, *Phys. Status Solidi B*, 2007, **244**, 2180–2189.
26 Y. Zorenko, V. Gorbenko, I. Konstankevych, A. Voloshinovskii, G. Stryganyuk, V. Mikhailin, V. Kolobanov and D. Spassky, *J. Lumin.*, 2005, **114**, 85–94.
27 E. Mihóková, M. Nikl, J. Mareš, A. Beitlerová, A. Vedda, K. Nejezchleb, K. Blažek and C. D'Ambrosio, *J. Lumin.*, 2007, **126**, 77–80.
28 L. Martinazzoli, S. Nargelas, P. Boháček, R. Calá, M. Dušek, J. Rohlíček, G. Tamulaitis, E. Auffray and M. Nikl, *Mater. Adv.*, 2022, **3**, 6842–6852.
29 S. Nargelas, A. Solovjovas, Y. Talochka, Y. Podlipskas, M. Kucera, Z. Lucenicova and G. Tamulaitis, *J. Mater. Chem. C*, 2023, **11**, 12007–12015.